

Inhibition of PIKfyve kinase prevents infection by Zaire ebolavirus and SARS-CoV-2

Yuan-Lin Kang^{1,2,3}, Yi-Ying Chou^{1,2,4}, Paul W. Rothlauf^{5,6}, Zhuoming Liu⁵, Timothy K. Soh⁶, David Cureton^{6,7}, James Brett Case⁸, Rita E. Chen⁸, Michael S. Diamond^{5,8}, Sean P. J. Whelan^{5,*}, Tom Kirchhausen^{1,2,9,*}

¹Department of Cell Biology, Harvard Medical School, 200 Longwood Av, Boston, MA 02115, USA

²Program in Cellular and Molecular Medicine, Boston Children's Hospital, 200 Longwood Av, Boston, MA 02115, USA

³Present Address: Department of Stem Cell and Regenerative Biology, Harvard University, 7 Divinity Ave, Cambridge, MA 02138, USA

⁴Present Address: Biogen, 225 Binney Street, Cambridge, MA 02142, USA

⁵Department of Molecular Microbiology, Washington University in Saint Louis, 660 South Euclid Avenue, Saint Louis, MI 63110, USA

⁶Program in Virology, Harvard Medical School, 200 Longwood Ave, Boston, MA 02115, USA

⁷Boehringer Ingelheim Animal Health, Inc. 3239 Satellite Blvd Duluth, GA 30096, USA

⁸Departments of Medicine and Pathology & Immunology, Washington University in Saint Louis, 660 South Euclid Avenue, Saint Louis, MI 63110, USA

⁹Department of Pediatrics, Harvard Medical School, 200 Longwood Av, Boston, MA 02115, USA

* Corresponding authors:

Dr. Tom Kirchhausen

Harvard Medical School

kirchhausen@crystal.harvard.edu

phone: 617.713.8888 / fax: 617.713.8898

Dr. Sean Whelan

spjwhelan@wustl.edu

Washington University in Saint Louis

phone: 314.286.1585

37 ***Running title:*** Drug inhibitors of ZEBOV and SARS-CoV-2 virus infection

38

39 ***Keywords:*** COVID-19, ZEBOV, SARS-CoV-2, inhibition, Apilimod, Vacuolin-1,
40 ***PIKfyve, pandemic***

41 **Virus entry is a multistep process. It initiates when the virus attaches to the host**
42 **cell and ends when the viral contents reach the cytosol. Genetically unrelated**
43 **viruses can subvert analogous subcellular mechanisms and use similar**
44 **trafficking pathways for successful entry. Antiviral strategies targeting early**
45 **steps of infection are therefore appealing, particularly when the probability for**
46 **successful interference through a common step is highest. We describe here**
47 **potent inhibitory effects on content release and infection by chimeric VSV**
48 **containing the envelope proteins of Zaire ebolavirus (VSV-ZEBOV) or SARS-CoV-**
49 **2 (VSV-SARS-CoV-2) elicited by Apilimod and Vacuolin-1, small molecule**
50 **inhibitors of the main endosomal Phosphatidylinositol-3-**
51 **Phosphate/Phosphatidylinositol 5-Kinase, PIKfyve. We also describe potent**
52 **inhibition of SARS-CoV-2 strain 2019-nCoV/USA-WA1/2020 by Apilimod. These**
53 **results define new tools for studying the intracellular trafficking of pathogens**
54 **elicited by inhibition of PIKfyve kinase and suggest the potential for targeting this**
55 **kinase in developing small-molecule antivirals against SARS-CoV-2.**

56 INTRODUCTION

57 Membrane-enveloped viruses deliver their contents to cells via envelope protein-
58 catalyzed membrane fusion. Binding of virus to specific host cell receptor(s) triggers
59 membrane fusion, which can occur directly at the plasma membrane or following
60 endocytic uptake. Viruses that require endocytic uptake can use different initial
61 trafficking routes to reach the site of membrane fusion. In endosomes, acidic pH serves
62 to triggers conformational rearrangements in the viral envelope proteins that catalyze
63 membrane fusion, as seen for influenza A virus (IAV) and vesicular stomatitis virus
64 (VSV). For Zaire ebolavirus (ZEBOV), proteolytic processing of the envelope protein by
65 host cell proteases (1) is necessary to expose the receptor binding domain prior to
66 engagement of Niemann-Pick disease type 1C (NPC1 or NPC Intracellular Cholesterol
67 Transporter 1) – the late endosomal-lysosomal receptor protein (2). Proteolytic
68 processing is also required for severe acute respiratory syndrome coronavirus (SARS-
69 CoV) (3, 4), and for the current pandemic SARS-CoV-2 (5). Lassa fever virus (LASV)
70 uses a different mechanism, binding alpha-dystroglycan at the plasma membrane (6),
71 for internalization with a subsequent pH-regulated switch that leads to engagement of
72 lysosomal associated membrane protein 1 (LAMP1) for membrane fusion (7).
73 Lymphocytic choriomeningitis virus (LCMV) also uses alpha-dystroglycan (6) and is
74 internalized in a manner that depends on endosomal sorting complexes required for
75 transport (ESCRT) proteins (8), although it remains unknown whether a second
76 receptor is required.

77
78 A hallmark of the endolysosomal system is controlled dynamic trafficking of vesicular
79 carriers among its various sub-compartments. Phosphoinositides are markers for
80 defining the identity of these sub-compartments because they are restricted in their
81 distribution to specific intracellular membranes [reviewed in (9)]. Although it is one of the
82 least abundant of the phosphoinositides in cells, PI(3,5)P2 is particularly important for
83 endomembrane homeostasis. It is produced by PIKfyve, which phosphorylates the D-5
84 position in phosphatidylinositol-3-phosphate (PI3P) to yield phosphatidylinositol 3,5-
85 bisphosphate (PI(3,5)P2) (10). First cloned as mammalian p235 (11), PIKfyve is a 240
86 kDa class III lipid kinase, present on the cytosolic face of endosomal membranes (12,
87 13) as part of a ternary complex with the PI(3,5)P2 5-phosphatase Sac3 and ArPIKfyve
88 (14).

89
90 Ablation of PIKfyve function by genetic (12, 15) or pharmacological means (16-20)
91 causes endosomal swelling and vacuolation of late endosomes and endolysosomes. It

92 is thought that these changes result from decreased membrane fission and concomitant
93 interference in endosomal traffic (13, 21). Small-molecule inhibitors of PIKfyve, all of
94 which have some structural resemblance to each other, have been studied as potential
95 drugs for treating cancer and autoimmune diseases. These inhibitors include Apilimod
96 (19), Vacuolin-1 (18), a series of 30 Vacuolin-related molecules (22), YM201636 (16),
97 and WX8 chemical family members (20). Physiological effects of these compound in
98 cells include inhibition of autophagy (17, 22, 23), reduced generation of IL-12/IL-23 (24),
99 and reduced dendritic cell infiltration in psoriasis (25).

100
101 Apilimod also inhibits infection by several viruses, including ZEBOV. Although it does
102 not alter the pH of endosomes nor inhibit cathepsin B or L (26), Apilimod blocks entry of
103 ZEBOV and other pathogenic filoviruses (27). Several groups reported that Apilimod
104 prevents colocalization of VSV-ZEBOV pseudoviruses with the ZEBOV endosomal
105 receptor NPC1, but does not prevent colocalization with early endosomal antigen 1
106 (EEA1) (5, 27, 28). Apilimod also inhibits entry of pseudotyped viruses bearing the spike
107 proteins of MERS-CoV, SARS-CoV, and SARS-CoV-2, as well as of authentic mouse
108 hepatitis virus (MHV) particles (5).

109
110 Here, we have studied the effects of Apilimod on infection of VSV-eGFP-SARS-CoV-2
111 and VSV-eGFP-ZEBOV chimeras and showed that Apilimod blocks infection of both,
112 with an IC₅₀ of ~50 nM. Apilimod and Vacuolin-1 also prevented entry and infection of
113 VSV-MeGFP-ZEBOV and many of the internalized VSV-MeGFP-ZEBOV virions
114 colocalized with NPC1 in the distended, vacuolated endosomes. This suggests that
115 blocking PIKfyve kinase has the same downstream effects on these viruses, even
116 though VSV-eGFP-SARS-CoV-2 does not require interaction with NPC1 for membrane
117 fusion. Apilimod also inhibits infection by authentic SARS-CoV-2 strain 2019-
118 nCoV/USA-WA1/2020 virus, with an IC₅₀ slightly lower than its IC₅₀ for the VSV-eGFP-
119 SARS-CoV-2. We suggest that Apilimod, which has passed safety tests in previous
120 human clinical trials for non-viral indications (24, 25, 29, 30), is a potential starting point
121 for developing small-molecule entry inhibitors of SARS-CoV-2 that could limit infection
122 and disease pathogenesis.

123 **RESULTS**

124 **Apilimod inhibits infection of VSV-MeGFP-LCMV and VSV-ZEBOV.** We inoculated
125 SVG-A cells with vesicular stomatitis virus (VSV) chimeras expressing the viral matrix
126 protein (M) fused to eGFP (MeGFP). The chimeras include VSV (VSV-MeGFP, which
127 initiates fusion at pH<6.2), VSV-V269H GP (VSV-MeGFP-V269H, a variant of VSV GP
128 that initiates fusion at pH<5.8), rabies virus GP (VSV-MeGFP-RABV), Lassa virus GP
129 (VSV-MeGFP-LASV), lymphocytic choriomeningitis virus GP (VSV-MeGFP-LCMV) or
130 Zaire Ebola virus GP (VSV-MeGFP-ZEBOV). Following the incubation protocol
131 summarized in **Fig 1A**, we tested the effects on infection of Apilimod or Vacuolin-1; both
132 compounds are small-molecule inhibitors of PIKfyve kinase, which generates PI(5)P
133 and PI(3,5)P2 in late endosomes and lysosomes. Using a flow cytometry based-assay
134 to monitor a single round of infection determined by expression of viral MeGFP (**Fig.**
135 **1B**), we found that Apilimod and Vacuolin-1 potently inhibit VSV-MeGFP-ZEBOV
136 infection (**Fig. 1C**). These results agree with results obtained by others with Apilimod
137 (26, 31) in different cell types infected with MLV virus pseudotyped with ZEBOV GP or
138 with Ebola virus itself (26, 27, 32). Apilimod was a less effective inhibitor of VSV-
139 MeGFP-LCMV infection, and Vacuolin-1 had no effect at the concentration used. In
140 contrast, Apilimod and Vacuolin-1 failed to prevent infection by VSV-MeGFP, VSV-
141 MeGFP-V269H, VSV-MeGFP-RABV, or VSV-MeGFP-LASV (**Fig. 1C**). IN1 (33), an
142 inhibitor of the phosphoinositide kinase Vps34, the main endosomal generator of PI3P,
143 also interfered with VSV-MeGFP-LCMV and VSV-MeGFP-ZEBOV infection (**Fig. 1C**).
144 All of these viruses require low pH to trigger viral membrane fusion with the endosomal
145 membranes, and as expected, infection was fully blocked by Bafilomycin A1, which
146 inhibits the vacuolar type H⁺-ATPase (V-ATPase) acidification activity (**Fig. 1C**).

147
148 **Apilimod and Vacuolin-1 prevent cytoplasmic entry of VSV-MeGFP-ZEBOV.**
149 Productive infection requires delivery of the viral ribonucleoprotein core (RNP) into the
150 cytosol. In these experiments, we deemed RNP delivery, as monitored by single cell
151 fluorescence microscopy imaging (experimental protocol summarized in **Fig. 2A** and
152 **3A**), to be successful when fluorescent MeGFP encapsulated in the incoming virus
153 appeared at the nuclear margin of infected cells. The representative examples of VSV
154 infection and RNP core release shown in **Fig. 2B** were obtained in the absence or
155 presence of cycloheximide, which prevents viral protein expression. In the absence of
156 cycloheximide (*left panel*), large amounts of newly synthesized MeGFP are present
157 throughout the cell. In the presence of cycloheximide (*right panel*), we observed MeGFP
158 in virions (fluorescent spots) as well as released MeGFP concentrated at the nuclear

159 margin. We scored the effect of Apilimod, Vacuolin-1 or IN1 on RNP delivery by VSV-
160 MeGFP, VSV-MeGFP-V269H and VSV-MeGFP-ZEBOV by determining the appearance
161 of MeGFP at the nuclear margin in cycloheximide-treated cells. Consistent with the
162 infection results, Apilimod, Vacuolin-1 and IN1 prevented entry of VSV-MeGFP-ZEBOV
163 but not of VSV-MeGFP or VSV-MeGFP-V269H. As expected, Bafilomycin A1 blocked
164 entry of all viruses (images in **Fig. 2C** and quantification in **Fig. 2D**).

165
166 **Intracellular trafficking of virus particles in the presence of Apilimod or Vacuolin-**
167 **1.** Internalized virus particles traffic along the endocytic pathway to reach the
168 endosomal compartment(s) from which membrane fusion and genome entry into the
169 cytosol occur. To establish the identity of the endosomal compartments, we used
170 genome-editing in SVG-A cells (**Figs. 3C, G and 4B, D**) to replace expression of a
171 subset of proteins enriched in different endosomal compartments (the small GTPases
172 Rab5c and Rab7a, EEA1, or NPC1) with their corresponding fluorescent chimeras
173 obtained by fusion with TagRFP, mScarlet, or Halo (**Figs. 3B, E, F, I, and 4C, E**). The
174 lack of fluorescently tagged filipin (a cholesterol binder) in the endolysosomal
175 compartment in the absence but not in the presence of U18666A, a potent inhibitor of
176 NPC1 (**Fig 4F**), showed that NPC1-Halo remained active as a cholesterol transporter.

177
178 Using live-cell spinning disk confocal microscopy (**Fig. 3, 4**), we monitored the presence
179 of virus particles in the fluorescently tagged endosomes by colocalization with the
180 fluorescent spots from the virus-incorporated MeGFP. We monitored entry by carrying
181 out the experiments in the presence of cycloheximide, thus ensuring that any MeGFP
182 fluorescent signal at the nuclear margin originated only from MeGFP molecules carried
183 by incoming viral particles (**Fig. 3B, F**). All cells were maintained at 37°C throughout all
184 phases of the experiment to ensure normal and undisturbed intracellular trafficking. All
185 control experiments performed in the absence of inhibitors showed arrival of VSV-
186 MeGFP, VSV-MeGFP-V269H, or VSV-MeGFP-ZEBOV virus particles to early (Rab5c
187 and EEA1) (**Fig. 3E, 4E**) or late endosomes and lysosomes (Rab7a or NPC1) (**Fig. 3I,**
188 **4C, E**). MeGFP released from all viruses appeared at the nuclear margin, showing
189 effective RNP release. NPC1, the receptor for VSV-MeGFP-ZEBOV entry is required for
190 fusion from endosomes (2). The successful VSV-MeGFP-ZEBOV infection observed in
191 the absence of drug in cells expressing NPC1-Halo alone or in combination with
192 mScarlet-EEA1 indicates that NPC1-Halo is capable of facilitating infection and that
193 VSV-MeGFP-ZEBOV trafficked to NPC1-Halo-containing endosomes.

194 Apilimod and Vacuolin-1 treatment of the SVG-A cells led to enlargement and
195 vacuolization of their endosomes and lysosomes tagged with fluorescent EEA1, Rab5c,
196 Rab7a or NPC1 (**Fig. 3-5**), in agreement with earlier PIKfyve ablation studies (13, 21).
197 VSV-MeGFP and VSV-MeGFP-V269H (fluorescent dots, white) reached all tagged
198 species of enlarged endolysosomes and successfully penetrated into the cytosol, as
199 indicated by MeGFP at the nuclear margin (**Fig. 3E, I**). VSV-MeGFP-ZEBOV also
200 trafficked to all tagged species of enlarged endolysosomes (**Fig. 3E, I**), often reaching
201 one of the numerous NPC1-containing vacuoles enriched in EEA1 (**Figs. 4E and 5B,C**).
202 VSV-MeGFP-ZEBOV in EEA1-containing endosomes increased in the presence of
203 Apilimod, as also reported for VLP ZEBOV (27). While able to reach NPC1-containing
204 functional endosomes in cells treated with Apilimod (**Fig. 4C, E and 5B, C**), VSV-
205 MeGFP-ZEBOV failed to penetrate into the cytoplasm, as reflected by absence of
206 MeGFP in the nuclear margin (**Fig. 2C, 3E, I, 4C,E and 5B**).

207
208 **Apilimod blocks infection of VSV SARS-CoV-2.** Using a recombinant vesicular
209 stomatitis virus (VSV) expressing soluble eGFP (VSV-eGFP) where the glycoprotein
210 (GP) was replaced with that of ZEBOV GP (VSV-eGFP-ZEBOV) or SARS-CoV-2 S
211 (VSV-eGFP-SARS-Cov2), we inoculated MA104 cells with these chimera viruses and
212 tested the effects of Apilimod on infection by flow cytometry (**Fig. 6A**). We found potent
213 inhibition of VSV-eGFP-SARS-CoV-2 infection by Apilimod and confirmed that the
214 compound also inhibits VSV-eGFP-ZEBOV infection (**Fig. 6B**). The dose-response
215 curves indicated similar effects for VSV-eGFP-ZEBOV and VSV-eGFP-SARS-CoV-2
216 (IC50s ~ 50 nM), in contrast to the absence of any detectable inhibition of VSV-eGFP
217 infection, used here as a negative control.

218
219 **Apilimod blocks infection of SARS-CoV-2 virus.**
220 To test the effect of Apilimod on bona fide SARS-CoV-2 infection, we exposed Vero E6
221 cells to fully infectious SARS-CoV-2 (strain 2019-nCoV/USA-WA1/2020); after 24 h
222 incubation, supernatants were harvested and tittered by focus-forming assay on a
223 separate set of Vero E6 cells (**Fig. 7A**). Apilimod strongly inhibited SARS-CoV-2
224 infection, and the dose-response curve was similar or more potent than those observed
225 for VSV-eGFP-ZEBOV or VSV-eGFP-SARS-CoV-2 (IC50s ~ 10 nM) (**Fig. 7B**).

226 **DISCUSSION**

227 Coronaviruses, filoviruses, and arenaviruses have different replication strategies and
228 unrelated surface glycoproteins that engage different receptor molecules during entry
229 (1, 2, 5-8). Coronavirus and filovirus surface glycoproteins share a requirement for
230 entry-associated proteolytic processing for activation as fusogens (1) Filoviruses require
231 passage through low pH compartments where cathepsins are active. Coronaviruses
232 may enter directly by fusion at the plasma membrane or following receptor mediated
233 endocytosis. Cell entry of SARS-CoV and SARS-CoV-2 depends on the protease
234 TMPRSS2 in conjunction with ACE2 (34-37), and when TMPRSS2 is present, the entry
235 pathway becomes insensitive to cathepsin inhibition (34, 37, 38).

236
237 The common inhibition of viruses from all three groups by Apilimod is a consequence of
238 perturbing their shared entry pathway. Moreover, it is not the cathepsin activity itself that
239 these compounds affect, judging from the outcome of the assays with Apilimod and
240 Vacuolin-1 showing they inhibit VSV chimeras bearing the surface glycoproteins of
241 ZEBOV and LCMV and to a lesser extent LASV. Apilimod also inhibits infection of cells
242 by VSV-SARS-CoV-2 as well as by authentic SARS-CoV-2; neither compound blocks
243 infection by wild-type VSV. For VSV-ZEBOV, we have shown that the virus reaches a
244 compartment enriched in NPC1, the ZEBOV co-receptor, and often also enriched in
245 EEA1, but that it nonetheless fails to release internal proteins into the cytosol. Apilimod
246 does not inhibit cathepsin (26) but Apilimod (39) and Vacuolin-1 (17, 23) can interfere
247 with cathepsin maturation as evidenced by an increase in pro-cathepsin in treated cells;
248 they do not influence endosomal pH (18, 26, 40) although other studies report Apilimod
249 decreases cathepsin activity (41) and Vacuolin-1 increases pH (17, 23). Irrespective of
250 this discrepancy, both Apilimod and Vacuolin-1 inhibit PI-3P-5-kinase (PIKfyve) (17, 19),
251 a three-subunit complex (14) with a PI-3P-binding FYVE domain (10, 11) that
252 recognizes the endosomal marker, PI-3-P. Functional ablation of this enzyme by
253 genetic means (12, 15) gives rise to the same cellular phenotype as treatment with
254 either compound (17-19). The similar dose-response curves for Apilimod inhibition of
255 the ZEBOV and SARS-CoV-2 chimeras (IC₅₀ of ~ 50 nM) and of authentic SARS-CoV-
256 2 virus (IC₅₀ ~ 10 nM) are in good agreement with the IC₅₀ of ~ 15 nM for Apilimod
257 inhibition of PIKfyve *in vitro* (19). Thus, perturbing normal endosomal trafficking by
258 inhibiting PIKfyve activity suggests it is the mechanism by which Apilimod and Vacuolin-
259 1 block entry of such a diverse set of viral pathogens.

260

261 One of the most striking consequence of PIKfyve inhibition, and hence of PI-3,5-P₂
262 restriction in endosomal membranes, is the swelling of endosomes into small, spherical
263 vacuoles - the phenomenon that gave Vacuolin-1 its name (18). Our imaging data with
264 VSV-MeGFP-ZEBOV chimeras show that the virus particles accumulating in these
265 structures, many of which also contain the NPC1 co-receptor (2, 42), often appear to be
266 relatively immobile and adjacent to the endosomal limiting membrane. One possible
267 explanation is that when a virion reaches these distended endosomes, it can bind or
268 remain bound to the limiting membrane, but not fuse. Another is that virions may fuse
269 with smaller intraluminal vesicles in the endosomal lumen (43), but that PI-3,5-P₂
270 depletion prevents back fusion of these vesicles with the endosomal limiting membrane
271 and inhibits release into the cytosol of the viral genome.

272
273 Inhibition of infection by authentic SARS-CoV-2 shows that the blocked release of the
274 viral genome from a vacuolated endosome is independent of the shape, size, and
275 distribution of spike protein on the virion. The assay we used to determine effects on
276 infectivity of authentic virus measured release of virions after multiple rounds of
277 infection, rather than entry, which we monitored in the VSV-SARS-CoV-2 experiments
278 by detecting eGFP synthesis in the cytosol. Nevertheless, the IC₅₀ of Apilimod in
279 experiments with authentic virus is remarkably similar (or even more potent) to that
280 obtained with chimeric VSV-SARS-CoV-2.

281
282 Although cathepsin L inhibitors block SARS-CoV and SARS-CoV-2 infection in cell
283 culture (4, 5), they have less pronounced effects when tested in animals (44). This may
284 because another protease, TMPRSS2 on the surface of cells in relevant tissues,
285 appears to prime SARS-CoV (44) and SARS-CoV-2 (37) spike proteins for efficient
286 entry. As the effectiveness of Apilimod and Vacuolin-1 does not depend on cathepsin
287 inhibition, their capacity to block entry of several distinct families of viruses is likely to be
288 independent and downstream of the protease that primes their surface glycoprotein for
289 fusion. Phase I and phase II clinical trials have shown that Apilimod is safe and well-
290 tolerated (24, 25, 29, 30). The trials were discontinued because of lack of effectiveness
291 against the autoimmune condition for which the drug was tested. We suggest that one
292 of these compounds, or a potential derivative, could be a candidate broad-spectrum
293 therapeutic for several emerging human viral pathogens, including SARS-CoV-2.

294 **FIGURE LEGENDS**

295 **Figure 1. Apilimod and Vacuolin-1 inhibit VSV-MeGFP-ZEBOV infection.**

296 **(A)** Schematic of infectivity assay, where SVG-A cells were pretreated for 1 h with 5 μ M
297 Vacuolin, 5 μ M Apilimod, 5 μ M IN1, or 10 nM BAF A1 and subsequently infected with
298 VSV-MeGFP (multiplicity of infection, MOI = 2), VSV-MeGFP-V269H (MOI = 1), VSV-
299 MeGFP-RABV (MOI = 0.6), VSV-MeGFP-LASV (MOI = 0.6), VSV-MeGFP-LCMV (MOI
300 = 0.6) or VSV-MeGFP-ZEBOV (MOI = 0.6) for 1 h in the presence of drugs. The cells
301 were then washed to remove unbound virus and incubated for the indicated times in the
302 presence of drugs. The cells were then fixed and the percentage of cells expressing
303 viral MeGFP was measured by flow cytometry.

304 **(B)** Representative flow cytometry results of an infection assay using VSV-MeGFP-
305 ZEBOV.

306 **(C)** Quantification of the infectivity is shown with averages from three independent
307 experiments per condition each determined as a duplicate measurement (error bars
308 show SEM). The statistical significance was determined using a one-way ANOVA and
309 Tukey *post-hoc* test (*, $P \leq 0.05$; **, $P \leq 0.01$; ***, $P \leq 0.001$).

310

311 **Figure 2. Apilimod and Vacuolin-1 inhibit VSV-MeGFP-ZEBOV.**

312 **(A)** Schematic of entry assay where SVG-A cells were infected with VSV-MeGFP (MOI
313 = 4), VSV-MeGFP-V269H (MOI = 4), or VSV-MeGFP-ZEBOV (MOI = 4). Experiments
314 were performed in the presence of 5 μ g/mL cycloheximide (CHX) to prevent protein
315 synthesis. Entry assay was based on the appearance of MeGFP fluorescence on the
316 nuclear margin on a per cell basis, of fixed infected cells visualized by fluorescence
317 microscopy. Staining the fixed cells with Alexa647 labeled wheat germ agglutinin
318 identified the plasma membrane of each cell (dashed outlines in **C**).

319 **(B)** Virus infection in the absence of CHX (left panel) resulted in the appearance of
320 MeGFP fluorescence throughout the cell volume. The presence of CHX resulted in virus
321 entry being observed by MeGFP fluorescence at the nuclear margin, which was
322 released from incoming viral particles (right panel, white arrows). Scale bar indicates 10
323 μ m.

324 **(C)** Representative examples of maximum-Z projection images from the whole cell
325 volume obtained with optical sections separated by 0.3 μ m using spinning disc confocal
326 microscopy. Scale bar indicates 10 μ m.

327 **(D)** Quantification of the number of cells with nuclear margin labeling from three
328 independent experiments each determined from fields containing 59-90 cells (error bars

329 show SEM). The statistical significance of the entry data was analyzed for statistical
330 significance by one-way ANOVA and Tukey *post-hoc* test (***, $P \leq 0.001$).

331
332 **Figure 3. Endolysosomal traffic of VSV-MeGFP-ZEBOV in cells expressing**
333 **TagRFP-Rab5c or TagRFP-Rab7a in the presence of Apilimod or Vacuolin-1.**
334 **(Associated Videos 1 and 2).**

335 **(A)** Schematic of live cell imaging experiment using SVG-A cells expressing
336 fluorescently tagged TagRFP-Rab5c or TagRFP-Rab7a. Cells were infected with VSV-
337 MeGFP, VSV-MeGFP-V269H or VSV-MeGFP-ZEBOV (MOI = 4). Viruses trafficking
338 (monitored with MeGFP) to the endo-lysosomal system (recognized by their labeling
339 with TagRFP-Rab5c or TagRFP-Rab7a) and virus entry (established by MeGFP at the
340 nuclear margin) were ascertained by live-cell fluorescence imaging using a spinning disc
341 confocal microscope.

342 **(B)** Visualization of VSV-MeGFP infection in TagRFP-Rab5c cells in the absence (left
343 panel) or presence of CHX (right panel, white arrows) using live-cell imaging. Scale bar
344 represents 10 μm .

345 **(C)** Genomic PCR analysis of SVG-A cells showing biallelic integration of TagRFP into
346 the *RAB5C* genomic locus by cotransfection of a plasmid coding for Cas9, a linear PCR
347 product coding for the specific gRNAs targeting a region near the ATG codon of Rab5c
348 under the control of the U6 promoter, and a template plasmid containing the RFP
349 sequence flanked by 800 base pairs upstream and downstream of the targeted region
350 (see materials and methods for more details) to generate a clonal gene-edited cell-line
351 expressing TagRFP-Rab5c.

352 **(D)** Quantification of VSV-MeGFP and VSV-MeGFP-ZEBOV colocalization with Rab5c
353 containing endosomes in the presence of CHX together with absence or presence of 5
354 μM Apilimod depicted in (E). Data shows number of viruses that colocalized with
355 endosomes containing or not Rab5c within the complete volume of the single cells
356 depicted in (e).

357 **(E)** Representative examples of maximum-Z projection images from four optical
358 sections spaced 0.35 μm apart of virus entry without or with IN1, Vacuolin, or Apilimod
359 for VSV-MeGFP (top), VSV-Me-GFP-V269H (middle), and VSV-MeGFP-ZEBOV
360 (bottom). Each condition is in the presence of CHX. All viruses reach Rab5c-containing
361 endosomes but only VSV-MeGFP-ZEBOV fails to penetrate in the presence of IN1,
362 Vacuolin-1, or Apilimod. Scale bars are 10 μm . Insets correspond to a single optical
363 section with scale bars of 3 μm .

364 **(F)** Visualization of VSV infection in TagRFP-Rab7a cells in the absence of CHX (left
365 panel) and entry in the presence of CHX (right panel, white arrows) with scale bar
366 indicating 10 μm .

367 **(G)** Genomic PCR analysis showing biallelic integration of TagRFP into the *RAB7A*
368 genomic locus to generate a clonal gene-edited cell-line expressing TagRFP-Rab7a,
369 using the same approach as used for *RAB5C*.

370 **(H)** Quantification of VSV-MeGFP and VSV-MeGFP-ZEBOV colocalization with Rab7a
371 containing endosomes in the presence of CHX with or without 5 μM Apilimod within the
372 complete cell volumes in the images depicted in (I).

373 **(I)** Representative examples of maximum-Z projection images from four optical sections
374 spaced 0.35 μm apart of virus entry without or with IN1, Vacuolin, or Apilimod for VSV-
375 MeGFP (top), VSV-Me-GFP-V269H (middle), and VSV-MeGFP-ZEBOV (bottom). All
376 viruses reach Rab7a-containing endosomes but only VSV-MeGFP-ZEBOV fails to
377 penetrate in the presence of IN1, Vacuolin-1 or Apilimod. Scale bars are 10 μm . Insets
378 correspond to a single optical section with scale bars of 3 μm .

379

380 **Figure 4. Endolysosomal traffic of VSV-MeGFP-ZEBOV in cells expressing NPC1-**
381 **Halo or coexpressing mScarlet-EEA1 and NPC1-Halo in the presence of Apilimod.**
382 **(Associated Video 3).**

383 **(A)** Schematic of live cell imaging experiment with gene-edited SVG-A cells expressing
384 NPC1-Halo or NPC1-Halo together with mScarlet-EEA1. Halo was labeled with either
385 JF549 or JF647. Cells were infected with VSV-MeGFP-ZEBOV (MOI = 3).

386 **(B)** Genomic PCR analysis showing biallelic integration of Halo into the *NPC1* genomic
387 locus to generate a clonal gene-edited cell-line expressing NPC1-Halo, using the same
388 approach as for *RAB5C* and *RAB7A*.

389 **(C)** Representative examples of maximum-Z projection images from four optical
390 sections spaced 0.25 μm apart in the absence (left) and presence of Apilimod (right)
391 showing that VSV-MeGFP-ZEBOV reached NPC1-Halo-containing endosomes even in
392 the presence of Apilimod, while failing to penetrate and infect. Scale bar indicates 10
393 μm . Insets correspond to a single optical section with the scale bar indicating 3 μm .

394 **(D)** SVG-A cells with genomic NPC1-Halo were further gene edited to contain EEA1
395 tagged with mScarlet. Genomic PCR analysis shows biallelic integration into the *EEA1*
396 locus of mScarlet-EEA1 (left) and into the *NPC1* locus of NPC1-Halo (right).

397 **(E)** Representative examples of maximum-Z projection images in the absence (left) and
398 presence of Apilimod (right) showing that VSV-MeGFP-ZEBOV reached endosomes
399 containing mScarlet-EEA1 and endosomes containing both mScarlet-EEA1 and NPC1-

400 Halo in the presence of Apilimod, while failing to penetrate and infect. Scale bar
401 indicates 10 μm . Insets correspond to a single optical section with scale bar indicating 3
402 μm .

403 **(F)** Representative images of parental (top) and gene-edited SVG-A cells expressing
404 NPC1-Halo (bottom) incubated with filipin III (naturally fluorescent polyene antibiotic
405 that binds to cholesterol) in the absence (left) and presence of U18666A (right, NPC1
406 inhibitor of cholesterol export) showing NPC1-Halo is a functional cholesterol
407 transporter.

408
409 **Figure 5. Extent of VSV-MeGFP-ZEBOV traffic into endosomes enriched in in**
410 **NPC1-Halo or NPC1-Halo and mScarlet-EEA1.**

411 **(A)** Schematic of imaging experiment of VSV-MeGFP-ZEBOV trafficking in NPC1-Halo
412 or NPC1-Halo and mScarlet-EEA1 gene edited SVG-A cells.

413 **(B)** Representative examples of maximum-Z projection images from four optical
414 sections spaced 0.25 μm apart in the absence and presence of Apilimod after 2 or 4
415 hours post infection. A large number of VSV-MeGFP-ZEBOV but not of VSV-MeGFP
416 particles accumulated in the endosomes enlarged upon Apilimod treatment.

417 **(C)** Quantification of VSV-MeGFP-ZEBOV colocalization with mScarlet-EEA1 alone,
418 both mScarlet-EEA1 and NPC1-Halo, or NPC1-Halo alone 2 and 4 hours post infection,
419 in the absence or presence of 5 μM Apilimod. Data obtained from complete cell volumes
420 are presented as numbers and corresponding % colocalization_s of VSV-MeGFP-
421 ZEBOV particles associated with a given type of endosome.

422
423 **Figure 6. Apilimod and Vacuolin-1 inhibit infection of VSV-eGFP-SARS-CoV-2**

424 **(A)** Schematic of infectivity assay of VSV-eGFP, VSV-eGFP-ZEBOV, and VSV-eGFP-
425 SARS-CoV-2 in MA104 cells. MA104 cells were pretreated for 1 h with the indicated
426 concentration Apilimod. Pretreated cells were inoculated with the indicated virus (MOI =
427 1) for 1 h at 37°C. At 6 hours post infection cells were harvested and the fraction of cell
428 expressing eGFP cells quantified by flow cytometry.

429 **(B)** Quantification of the infectivity is shown with averages +/- SEM from three
430 independent experiments. Statistical significance was determined using a T-test (*, $P \leq$
431 0.05; **, $P \leq 0.01$).

432
433 **Figure 7. Apilimod inhibits infection of SARS-CoV-2 virus**

434 **(A)** Schematic of infectivity assay of fully infectious Sars-CoV-2 (strain 2019-nCoV/USA-
435 WA1/2020). Vero E6 cell monolayers were pretreated with medium containing DMSO

436 or serial dilutions of Apilimod at the indicated concentrations. SARS-CoV-2 was diluted
437 (MOI = 0.01) in Apilimod-containing medium and added to Vero E6 cells for 1 h at 37°C.
438 After adsorption, the viral inocula were removed, and medium containing the respective
439 concentration of Apilimod was reapplied. After 24 h incubation, supernatants were
440 harvested and titrated by focus-forming assay on a separate set of Vero E6 cells.

441 **(B)** Quantification of the infectivity is shown with averages +/- SEM from three
442 independent experiments per condition and expressed as the percent infection relative
443 to mock-treated SARS-CoV-2 infected cells.

444

445 **Table I. Primer sequences used to generate the sgRNAs and corresponding**
446 **genomic fragments.**

447

448 **Table II. Primer sequences used for screening.**

449

450 **Video 1. Apilimod doesn't inhibit VSV-MeGFP entry.** Maximal Z-projection from four
451 optical sections separated 0.25 μm apart of SVG-A cells gene-edited to express
452 TagRFP-Rab5c imaged by spinning disc confocal microscopy every 3 seconds for 3
453 min. Cells were infected with VSV-MeGFP (MOI = 4) in the presence of CHX with or
454 without 5 μM Apilimod and imaged ~ 3-4 h post-infection.

455

456 **Video 2. Apilimod inhibits VSV-MeGFP-ZEBOV entry.** Maximal Z-projection from four
457 optical sections separated 0.25 μm apart of SVG-A cells gene-edited to express
458 TagRFP-Rab5c imaged by spinning disc confocal microscopy every 3 seconds for 3
459 min. Cells were infected with VSV-MeGFP-ZEBOV (MOI = 3) in the presence of CHX
460 with or without 5 μM Apilimod and imaged ~ 6-7 h post infection.

461

462 **Video 3. Apilimod inhibits VSV-MeGFP-ZEBOV entry.** Maximal Z-projection from four
463 optical sections separated 0.25 μm apart of SVG-A cells gene-edited to express NPC1-
464 Halo imaged by spinning disc confocal microscopy every 3 seconds for 3 min. Cells
465 were infected with VSV-MeGFP-ZEBOV (MOI = 3) with or without 5 μM Apilimod and
466 imaged ~ 5 h post infection.

467 **MATERIAL AND METHODS**

468 **Cell culture**

469 Human astroglial SVG-A derived cells (a kind gift from Walter J. Atwood) were grown at
470 37°C and 5% CO₂ in Minimum Essential Medium (MEM) (10-010-CV; Corning)
471 supplemented with 10% heat inactivated fetal bovine serum (S11150; Atlanta
472 Biologicals), penicillin and streptomycin (1406-05-9; VWR International). African Green
473 Monkey kidney epithelial MA104 cells (a kind gift from Siyuan Ding, WUSM) were grown
474 at 37°C and 5% CO₂ in Medium 199 supplemented with 10% heat inactivated fetal
475 bovine serum. Vero C1008 [Vero 76, clone E6, Vero E6] (ATCC CRL-1586) cells were
476 cultured in Dulbecco's Modified Eagle Medium (DMEM) supplemented with 10% fetal
477 bovine serum, and penicillin and streptomycin. Vero CCL-81 (ATCC CCL-81) cells were
478 maintained in DMEM supplemented with 10% FBS, 10mM HEPES pH 7.4, 1%
479 Glutamax, and penicillin/streptomycin.

480

481 **Reagents**

482 Vacuolin-1 (18) was custom synthesized; Apilimod (HY-14644) was from MedChem
483 Express, IN1 was a kind gift from Dr. N. Gray (33), U-18666A (10009085), and Filipin III
484 (70440) were from Cayman Chemical, Bafilomycin A1 (B1793-2UG) was from Sigma-
485 Aldrich, Cycloheximide (239764) was from Calbiochem, and wheat germ agglutinin
486 conjugated with Alexa Fluor®-647 (W32466) was from ThermoFisher.

487

488 **Viruses**

489 Recombinant VSV (Indiana serotype) expressing MeGFP alone which initiates fusion at
490 pH<6.2 (VSV-MeGFP) (45) (or in combination with V269H GP, VSV-MeGFP-V269H),
491 RABV GP (VSV-MeGFP-RABV) (46), LASV GP (VSV-MeGFP-LASV) (7), LCMV GP
492 (VSV-MeGFP-LCMV), Zaire EBOV GP (VSV-MeGFP-ZEBOV) (47) or SARS-CoV-2 S
493 Wuhan-Hu-1 strain (VSV-eGFP-SARS-CoV-2 – description to be published elsewhere)
494 were used for infection, entry and live cell imaging assays. All viruses were generated
495 and recovered according to (48).

496

497 SARS-CoV-2 strain 2019-nCoV/USA-WA1/2020 was obtained from the Centers for
498 Disease Control and Prevention (gift of Natalie Thornburg). Virus was passaged once in
499 Vero CCL81 cells (ATCC) and titrated by focus-forming assay also on Vero E6 cells.

500

501 **Genome-editing**

502 Individual cell lines of SVG-A were gene edited in both alleles using the CRISPR/Cas9
503 system to incorporate fluorescent tags into the N-terminus of Rab5c (TagRFP), Rab7a
504 (TagRFP), EEA1 (mScarlet) or the C-terminus of NPC1 (Halo). The NPC1-Halo
505 expressing cells were further gene edited to incorporate mScarlet-EEA1 creating SVG-A
506 cells simultaneously expressing mScarlet-EEA1 and NPC1-Halo.

507
508 A free PCR strategy (49, 50) was used to generate small guide RNAs (sgRNA) with
509 target sequences for either Rab5c, Rab7a, NPC1, or EEA1.

510
511 The genomic DNA fragment of Rab5c, Rab7a, NPC1, or EEA1 genes fused with either
512 TagRFP, Halo, or mScarlet were cloned into the pUC19 vector (donor constructs) which
513 then served as homologous recombination repair templates for the Cas9 enzyme-
514 cleaved genomic DNA. Donor constructs were obtained by a ligation of PCR
515 amplification products from the genomic DNA fragments, TagRFP, Halo, and mScarlet
516 sequences. Primers F1-R1 and F3-R3 amplified approximately 800 base pairs of
517 genomic sequences upstream and downstream of the start codon of Rab5c, Rab7a or
518 EEA1, or the stop codon of NPC1, respectively. Primers F1 and R3 contain sequences
519 complementary to the pUC19 vector linearized using the SmaI restriction enzyme (lower
520 case in the primer sequences). The TagRFP sequence containing the GGS peptide
521 linker was amplified using primers F2-R2 from a TagRFP mammalian expression
522 plasmid used as a template. The F2 primer contains complementary sequences to the
523 3' end of the F1-R1 fragment, while the F3 primer contains complementary sequences
524 to the 3' end of the TagRFP sequences. Primer sequences used to generate the
525 sgRNAs and corresponding genomic fragments are listed in Table I; primers used for
526 screening are listed in Table II.

527
528 PCR products (fragments F1-R1, F2-R2, and F3-R3) were subjected to electrophoresis
529 in 1% agarose and gel purified using a purification kit from Zymogen. The PCR
530 fragments were cloned into the linearized pUC19 vector using the Gibson Assembly
531 Cloning Kit (E5510S; New England Biolabs).

532
533 SVG-A cells (1.5×10^5 cells) were co-transfected with 0.8 μg of *Streptococcus*
534 *pyogenes* Cas9, 0.8 μg free PCR product coding for the target sgRNA, and 0.8 μg
535 pUC19 vector using Lipofectamine 2000 reagent (Invitrogen) according to the
536 manufacturer's instructions. Transfected cells were grown for 7 to 10 days and sorted
537 for TagRFP, Halo, or mScarlet expression using fluorescence-activated cell sorting

538 (FACS) (SH-800S; Sony). Prior to FACS, NPC1-Halo cells were labeled for 15 minutes
539 with Janelia FluorTM 647 (JF647). Single cells expressing the desired chimera were
540 isolated, clonally expanded, and then screened by genomic PCR for TagRFP, Halo, or
541 mScarlet insertion into both alleles.

542

543 **Infection assays**

544 SVG-A cells were plated at about 30-40% confluency into 24-well plates and incubated
545 for 1 day at 37°C and 5% CO₂. At the start of the experiment, cells were incubated with
546 the indicated drug or DMSO at 37°C for one hour. Following this, cells were incubated
547 for 1 h at 37°C with VSV, VSV-MeGFP-V269H, VSV-MeGFP-RABV, VSV-MeGFP-
548 LASV, VSV-MeGFP-LCMV or VSV-MeGFP-ZEBOV in drug or DMSO-containing
549 infection medium (α -MEM, 50mM HEPES, 2% FBS). Cells were then washed to remove
550 non-adsorbed viruses and further incubated at 37°C in medium containing the drug or
551 DMSO with experiments ending at the indicated times by fixation with 3.7%
552 formaldehyde in PBS. Fluorescent intensity from 20,000 single cells from a single round
553 of infection was determined by flow cytometry using a BD FACSCantoTM II equipped
554 with DIVA software package.

555

556 MA104 cells were pretreated for 1 h with the indicated concentration Apilimod or DMSO.
557 Pretreated cells were inoculated with VSV-eGFP, VSV-eGFP-ZEBOV or VSV-eGFP-
558 SARS-CoV-2 at an MOI = 1 (based on titers in MA104 cells) in the presence of Apilimod
559 or DMSO for 1 h at 37°C. Six to 8 h post infection, cells were collected and fixed in 2%
560 PFA and then subjected to flow cytometry. The percentage of GFP cells was
561 determined using FlowJo software (Tree Star Industries, Ashland, OR).

562

563 Vero E6 cell monolayers were pretreated for 1 h at 37°C with serial dilutions of Apilimod
564 at the indicated concentrations. Next, SARS-CoV-2 was diluted to an MOI of 0.01 focus-
565 forming units (FFU)/cell in Apilimod-containing medium and added to Vero E6 cells for 1
566 h at 37°C. After adsorption, cells were washed once with PBS, and medium containing
567 the respective concentration of Apilimod was added. Cell were incubated for a 24 h at
568 37°C, and at which time cell culture supernatants were removed and used for
569 determination of viral titer by focus forming assay.

570

571 **SARS-CoV-2 focus forming assay**

572 Cell culture supernatants from virus-infected cells were diluted serially 10-fold and
573 added to Vero E6 cell monolayers in 96-well plates and incubated at 37°C for 1 h.

574 Subsequently, cells were overlaid with 1 % (w/v) methylcellulose in MEM supplemented
575 with 2% FBS. Plates were harvested 30 h later by removing overlays and fixed with 4%
576 paraformaldehyde in PBS for 20 min at room temperature. Plates were washed and
577 sequentially incubated with 1 µg/mL of CR3022 anti-spike antibody (51) and HRP-
578 conjugated goat anti-human IgG in PBS supplemented with 0.1% saponin and 0.1%
579 BSA. SARS-CoV-2-infected cell foci were visualized using TrueBlue peroxidase
580 substrate (KPL) and quantitated on an ImmunoSpot microanalyzer (Cellular
581 Technologies). Data were processed using Prism software (GraphPad Prism 8.0) and
582 viral titers are reported as percent inhibition relative to mock-treated SARS-CoV-2
583 infected cells.

584

585 **Entry assay and intracellular traffic**

586 SVG-A cells plated on glass #1.5 coverslips at about 30-40% confluency one day prior
587 to experiment were treated with drug or DMSO for 1 h at 37°C. Following this, cells
588 were incubated at 37°C with VSV, VSV-MeGFP-V269H, VSV-MeGFP-RABV, VSV-
589 MeGFP-LASV, VSV-MeGFP-LCMV or VSV-MeGFP-ZEBOV in drug or DMSO
590 containing infection medium. After this, cells were washed then further incubated in
591 medium containing the drug or DMSO at 37°C with the experiment ending at the
592 indicated time by fixation for 20 min at room temperature with 3.7% formaldehyde in
593 PBS. This was followed with a 10-min incubation of 5 µg/mL of Alexa647-labeled wheat
594 germ agglutinin in PBS to label the outline of the cells.

595

596 Cells were imaged using a spinning disk confocal microscope with optical planes
597 spaced 0.3 µm apart (52). The entry assay scored the presence of MeGFP at the
598 nuclear margin in each cell. Trafficking of viruses to endosomal compartments was
599 observed using live-cell imaging using the spinning disc confocal microscope. Chemical
600 fixation tends to eliminate the large endolysosomal vacuoles generated by Vacuolin-1 or
601 Apilimod and reduces the colocalization with viral particles contained within. Time series
602 with images taken every 3 seconds for 3 min in a single optical plane with the
603 appropriate fluorescent channels (52) were acquired from non-fixed samples imaged at
604 the end of the experimental period. For experiments containing NPC1-Halo, the Halo-
605 tagged cells were labeled with either 250 nM JF549 or JF647 dye in media for 30 min at
606 37°C. Following labeling, cells were washed three times with media. The microscope
607 was operated using the Slidebook 6.4 software package (31) and images were displayed
608 also using this software.

609

610 **Statistical tests**

611 To compare the means from cells with different treatments, one-way ANOVA and the
612 *post-hoc* Tukey test analysis were used to take into account unequal sample sizes as
613 indicated in figure legends.

614 **ACKNOWLEDGEMENTS**

615 We thank Walter J. Atwood for providing the parental SVG-A cells, Eric Marino, Justin
616 H. Houser and Tegye John Vadakkan for maintaining the spinning disc confocal
617 microscope (T.K. Lab), Marina Cella and Erica Lantelme from the flow cytometry facility,
618 Department of Pathology and Immunology, WUSM for help with flow cytometry,
619 Stephen C. Harrison for helpful discussions and editorial assistance and Alex J. B.
620 Kreutzberger for editorial help. This research was supported by National Institutes of
621 Health funding (AI109740) to S.P.W. and T.K., by MIRA NIH award (GM130386) to T.K.,
622 by National Institutes of Health funding (AI059371) and unrestricted funds from WUSM
623 to S.P.W. and by (75N93019C00062 and R01 AI127828) to M.S.D.

624

625 **AUTHOR CONTRIBUTIONS (NAMES GIVEN AS INITIALS)**

626 T.K., S.P.W., and M.S.D. were responsible for the overall design of the study; Y.K.
627 carried out virus infection, entry and imaging experiments and prepared figures in the
628 lab of T.K. (Fig. 1-5). P.W.R. designed, generated and characterized VSV-eGFP-
629 SARS-CoV-2 and Z.L. carried out VSV-chimera infection experiments in the lab of
630 S.P.W. (Fig. 6). J.B.C. and R.E.C. carried out the experiments with authentic SARS-
631 CoV-2 under BSL3 conditions in the lab of M.S.D. (Fig. 7). Recombinant viruses were
632 generated and characterized by D.K.C., S.P., M.R and T.S. in the lab of S.P.W; T.K.
633 drafted the manuscript and editorially reviewed it in close association with SP.W. and
634 M.S.D; the authors commented on the manuscript.

635

636 **COMPETING FINANCIAL INTEREST STATEMENT**

637 M.S.D. is a consultant for Inbios, Vir Biotechnology, NGM Biopharmaceuticals, and on
638 the Scientific Advisory Board of Moderna. The Diamond laboratory at Washington
639 University School of Medicine has received sponsored research agreements from
640 Moderna and Emergent BioSolutions.

641 **REFERENCES**

- 642 1. Chandran K, Sullivan NJ, Felbor U, Whelan SP, Cunningham JM (2005)
643 Endosomal proteolysis of the Ebola virus glycoprotein is necessary for infection.
644 308(5728):1643–1645.
- 645 2. Carette JE, et al. (2011) Ebola virus entry requires the cholesterol transporter
646 Niemann-Pick C1. *Nature* 477(7364):340–343.
- 647 3. Huang I-C, et al. (2006) SARS coronavirus, but not human coronavirus NL63,
648 utilizes cathepsin L to infect ACE2-expressing cells. *J Biol Chem* 281(6):3198–
649 3203.
- 650 4. Simmons G, et al. (2005) Inhibitors of cathepsin L prevent severe acute
651 respiratory syndrome coronavirus entry. *Proc Natl Acad Sci USA* 102(33):11876–
652 11881.
- 653 5. Ou X, et al. (2020) Characterization of spike glycoprotein of SARS-CoV-2 on virus
654 entry and its immune cross-reactivity with SARS-CoV. *Nat Commun* 11(1):1–12.
- 655 6. Cao W, et al. (1998) Identification of alpha-dystroglycan as a receptor for
656 lymphocytic choriomeningitis virus and Lassa fever virus. *Science*
657 282(5396):2079–2081.
- 658 7. Jae LT, et al. (2014) Virus entry. Lassa virus entry requires a trigger-induced
659 receptor switch. *Science* 344(6191):1506–1510.
- 660 8. Pasqual G, Rojek JM, Masin M, Chatton J-Y, Kunz S (2011) Old world
661 arenaviruses enter the host cell via the multivesicular body and depend on the
662 endosomal sorting complex required for transport. *PLoS Pathog* 7(9):e1002232.
- 663 9. Carlton JG, Cullen PJ (2005) Coincidence detection in phosphoinositide signaling.
664 *Trends Cell Biol* 15(10):540–547.
- 665 10. Sbrissa D, Ikononov OC, Shisheva A (1999) PIKfyve, a mammalian ortholog of
666 yeast Fab1p lipid kinase, synthesizes 5-phosphoinositides. Effect of insulin. *J Biol*
667 *Chem* 274(31):21589–21597.
- 668 11. Shisheva A, Sbrissa D, Ikononov O (1999) Cloning, characterization, and

- 669 expression of a novel Zn²⁺-binding FYVE finger-containing phosphoinositide
670 kinase in insulin-sensitive cells. *Mol Cell Biol* 19(1):623–634.
- 671 12. Ikonov OC, Sbrissa D, Shisheva A (2001) Mammalian cell morphology and
672 endocytic membrane homeostasis require enzymatically active phosphoinositide
673 5-kinase PIKfyve. *J Biol Chem* 276(28):26141–26147.
- 674 13. Rutherford AC, et al. (2006) The mammalian phosphatidylinositol 3-phosphate 5-
675 kinase (PIKfyve) regulates endosome-to-TGN retrograde transport. *J Cell Sci*
676 119(Pt 19):3944–3957.
- 677 14. Sbrissa D, et al. (2007) Core protein machinery for mammalian
678 phosphatidylinositol 3,5-bisphosphate synthesis and turnover that regulates the
679 progression of endosomal transport. Novel Sac phosphatase joins the ArPIKfyve-
680 PIKfyve complex. *J Biol Chem* 282(33):23878–23891.
- 681 15. Ikonov OC, et al. (2002) Functional dissection of lipid and protein kinase
682 signals of PIKfyve reveals the role of PtdIns 3,5-P₂ production for endomembrane
683 integrity. *J Biol Chem* 277(11):9206–9211.
- 684 16. Jefferies HBJ, et al. (2008) A selective PIKfyve inhibitor blocks PtdIns(3,5)P₂
685 production and disrupts endomembrane transport and retroviral budding. *EMBO*
686 *Rep* 9(2):164–170.
- 687 17. Sano O, et al. (2016) Vacuolin-1 inhibits autophagy by impairing lysosomal
688 maturation via PIKfyve inhibition. *FEBS Lett* 590(11):1576–1585.
- 689 18. Cerny J, et al. (2004) The small chemical vacuolin-1 inhibits Ca²⁺-dependent
690 lysosomal exocytosis but not cell resealing. *EMBO Rep* 5(9):883–888.
- 691 19. Cai X, et al. (2013) PIKfyve, a class III PI kinase, is the target of the small
692 molecular IL-12/IL-23 inhibitor apilimod and a player in Toll-like receptor signaling.
693 *Chem Biol* 20(7):912–921.
- 694 20. Sharma G, et al. (2019) A family of PIKfyve inhibitors with therapeutic potential
695 against autophagy-dependent cancer cells disrupt multiple events in lysosome
696 homeostasis. *Autophagy* 15(10):1694–1718.
- 697 21. Ikonov OC, et al. (2003) Active PIKfyve associates with and promotes the

- 698 membrane attachment of the late endosome-to-trans-Golgi network transport
699 factor Rab9 effector p40. *J Biol Chem* 278(51):50863–50871.
- 700 22. Chen C, et al. (2017) Identification of Novel Vacuolin-1 Analogues as Autophagy
701 Inhibitors by Virtual Drug Screening and Chemical Synthesis. *Molecules*
702 22(6):891.
- 703 23. Lu Y, et al. (2014) Vacuolin-1 potently and reversibly inhibits autophagosome-
704 lysosome fusion by activating RAB5A. *Autophagy* 10(11):1895–1905.
- 705 24. Sands BE, et al. (2010) Randomized, double-blind, placebo-controlled trial of the
706 oral interleukin-12/23 inhibitor apilimod mesylate for treatment of active Crohn's
707 disease. *Inflamm Bowel Dis* 16(7):1209–1218.
- 708 25. Wada Y, et al. (2012) Apilimod inhibits the production of IL-12 and IL-23 and
709 reduces dendritic cell infiltration in psoriasis. *PLoS ONE* 7(4):e35069.
- 710 26. Nelson EA, et al. (2017) The phosphatidylinositol-3-phosphate 5-kinase inhibitor
711 apilimod blocks filoviral entry and infection. *PLoS Negl Trop Dis* 11(4):e0005540.
- 712 27. Qiu S, et al. (2018) Ebola virus requires phosphatidylinositol (3,5) bisphosphate
713 production for efficient viral entry. *Virology* 513:17–28.
- 714 28. Spence JS, Krause TB, Mittler E, Jangra RK, Chandran K (2016) Direct
715 Visualization of Ebola Virus Fusion Triggering in the Endocytic Pathway. *MBio*
716 7(1):e01857–15.
- 717 29. Burakoff R, et al. (2006) A phase 1/2A trial of STA 5326, an oral interleukin-12/23
718 inhibitor, in patients with active moderate to severe Crohn's disease. *Inflamm*
719 *Bowel Dis* 12(7):558–565.
- 720 30. Krausz S, et al. (2012) Brief report: a phase IIa, randomized, double-blind,
721 placebo-controlled trial of apilimod mesylate, an interleukin-12/interleukin-23
722 inhibitor, in patients with rheumatoid arthritis. *Arthritis Rheum* 64(6):1750–1755.
- 723 31. Hulseberg CE, et al. (2019) Arbidol and Other Low-Molecular-Weight Drugs That
724 Inhibit Lassa and Ebola Viruses. *J Virol* 93(8):11.
- 725 32. Dyall J, et al. (2018) Identification of Combinations of Approved Drugs With

- 726 Synergistic Activity Against Ebola Virus in Cell Cultures. *J Infect Dis*
727 218(suppl_5):S672–S678.
- 728 33. Bago R, et al. (2014) Characterization of VPS34-IN1, a selective inhibitor of
729 Vps34, reveals that the phosphatidylinositol 3-phosphate-binding SGK3 protein
730 kinase is a downstream target of class III phosphoinositide 3-kinase. *Biochem J*
731 463(3):413–427.
- 732 34. Glowacka I, et al. (2011) Evidence that TMPRSS2 activates the severe acute
733 respiratory syndrome coronavirus spike protein for membrane fusion and reduces
734 viral control by the humoral immune response. *J Virol* 85(9):4122–4134.
- 735 35. Shulla A, et al. (2011) A transmembrane serine protease is linked to the severe
736 acute respiratory syndrome coronavirus receptor and activates virus entry. *J Virol*
737 85(2):873–882.
- 738 36. Matsuyama S, et al. (2010) Efficient activation of the severe acute respiratory
739 syndrome coronavirus spike protein by the transmembrane protease TMPRSS2. *J*
740 *Virol* 84(24):12658–12664.
- 741 37. Hoffmann M, et al. (2020) SARS-CoV-2 Cell Entry Depends on ACE2 and
742 TMPRSS2 and Is Blocked by a Clinically Proven Protease Inhibitor. *Cell*
743 181(2):271–280.e8.
- 744 38. Simmons G, et al. (2004) Characterization of severe acute respiratory syndrome-
745 associated coronavirus (SARS-CoV) spike glycoprotein-mediated viral entry. *Proc*
746 *Natl Acad Sci USA* 101(12):4240–4245.
- 747 39. Gayle S, et al. (2017) Identification of apilimod as a first-in-class PIKfyve kinase
748 inhibitor for treatment of B-cell non-Hodgkin lymphoma. *Blood* 129(13):1768–
749 1778.
- 750 40. Nelson CDS, Derdowski A, Maginnis MS, O'Hara BA, Atwood WJ (2012) The VP1
751 subunit of JC polyomavirus recapitulates early events in viral trafficking and is a
752 novel tool to study polyomavirus entry. *Virology* 428(1):30–40.
- 753 41. Baranov MV, et al. (2019) The Phosphoinositide Kinase PIKfyve Promotes
754 Cathepsin-S-Mediated Major Histocompatibility Complex Class II Antigen
755 Presentation. *iScience* 11:160–177.

- 756 42. Côté M, et al. (2011) Small molecule inhibitors reveal Niemann-Pick C1 is
757 essential for Ebola virus infection. *Nature* 477(7364):344–348.
- 758 43. Le Blanc I, et al. (2005) Endosome-to-cytosol transport of viral nucleocapsids. *Nat*
759 *Cell Biol* 7(7):653–664.
- 760 44. Zhou Y, et al. (2015) Protease inhibitors targeting coronavirus and filovirus entry.
761 *Antiviral Res* 116:76–84.
- 762 45. Soh TK, Whelan SPJ (2015) Tracking the Fate of Genetically Distinct Vesicular
763 Stomatitis Virus Matrix Proteins Highlights the Role for Late Domains in
764 Assembly. 89(23):11750–11760.
- 765 46. Piccinotti S, Kirchhausen T, Whelan SPJ (2013) Uptake of rabies virus into
766 epithelial cells by clathrin-mediated endocytosis depends upon actin.
767 87(21):11637–11647.
- 768 47. Wong AC, Sandesara RG, Mulherkar N, Whelan SP, Chandran K (2010) A
769 forward genetic strategy reveals destabilizing mutations in the Ebolavirus
770 glycoprotein that alter its protease dependence during cell entry. *J Virol*
771 84(1):163–175.
- 772 48. Whelan SP, Ball LA, Barr JN, Wertz GT (1995) Efficient recovery of infectious
773 vesicular stomatitis virus entirely from cDNA clones. *Proc Natl Acad Sci USA*
774 92(18):8388–8392.
- 775 49. Ran FA, et al. (2013) Genome engineering using the CRISPR-Cas9 system. *Nat*
776 *Protoc* 8(11):2281–2308.
- 777 50. Chou Y-Y, et al. (2016) Identification and characterization of a novel broad
778 spectrum virus entry inhibitor. 90(9):4494–4510.
- 779 51. Yuan M, et al. (2020) A highly conserved cryptic epitope in the receptor-binding
780 domains of SARS-CoV-2 and SARS-CoV. *Science*:eabb7269.
- 781 52. Cocucci E, Aguet F, Boulant S, Kirchhausen T (2012) The first five seconds in the
782 life of a clathrin-coated pit. 150(3):495–507.

783

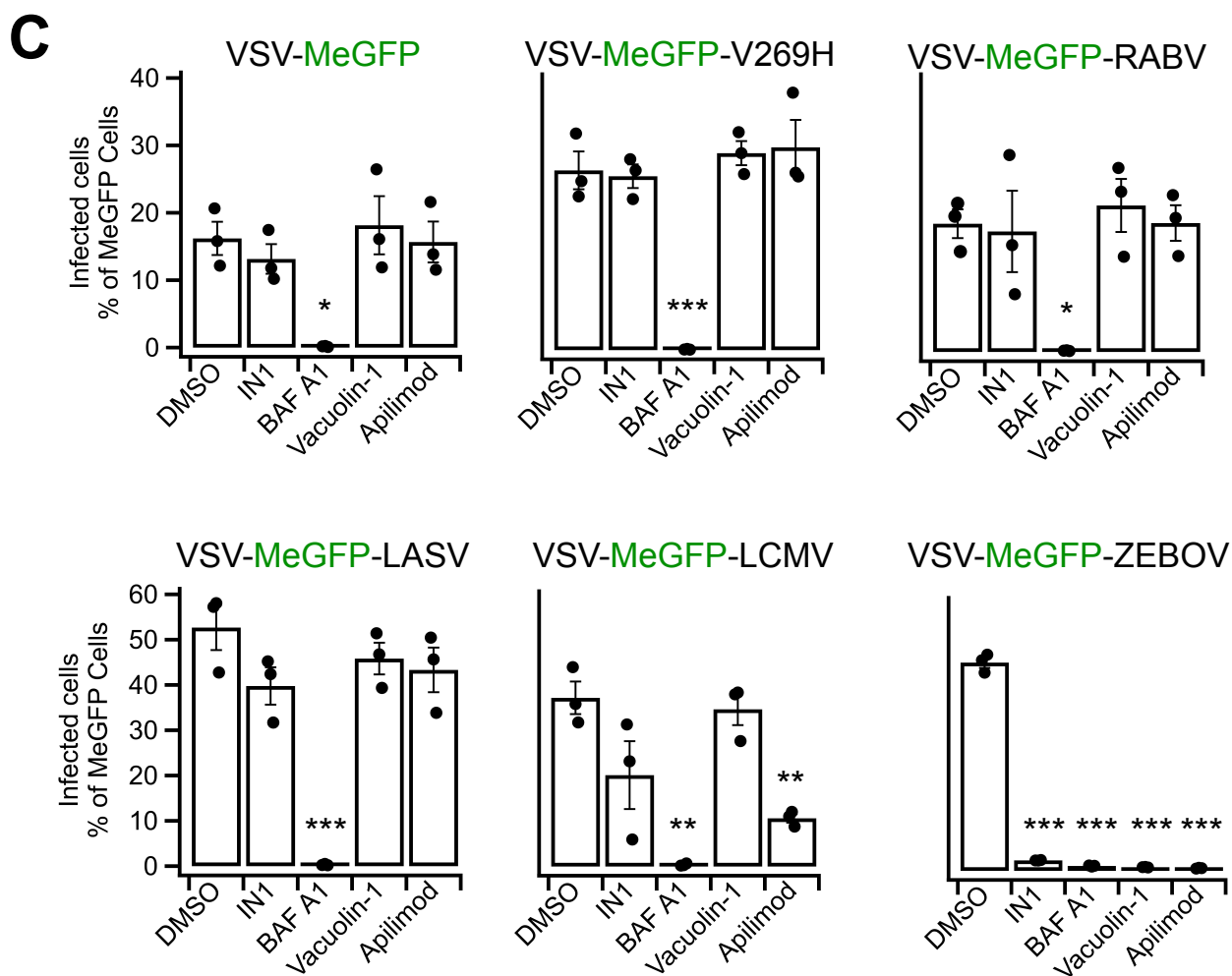
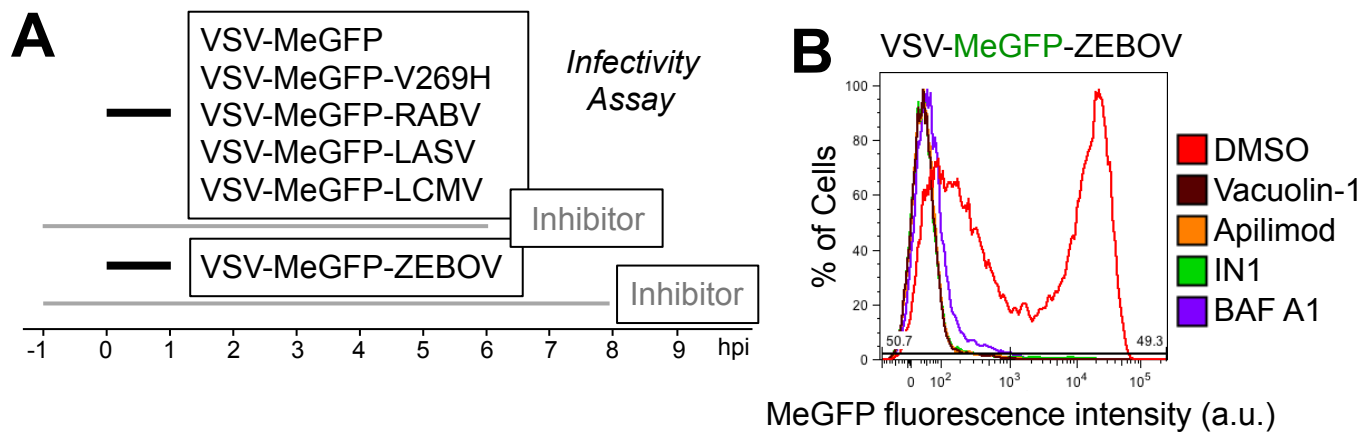


Figure 1

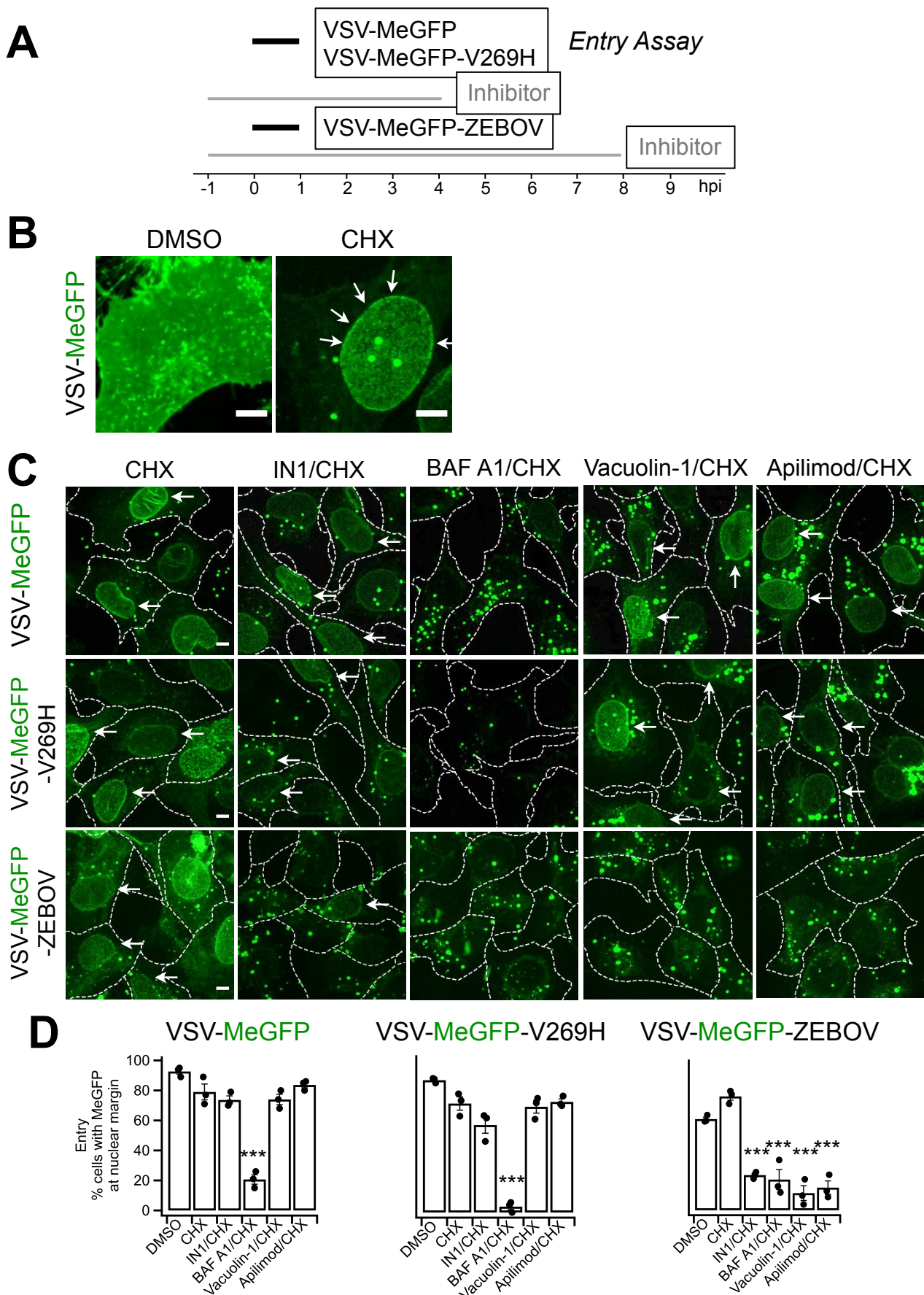
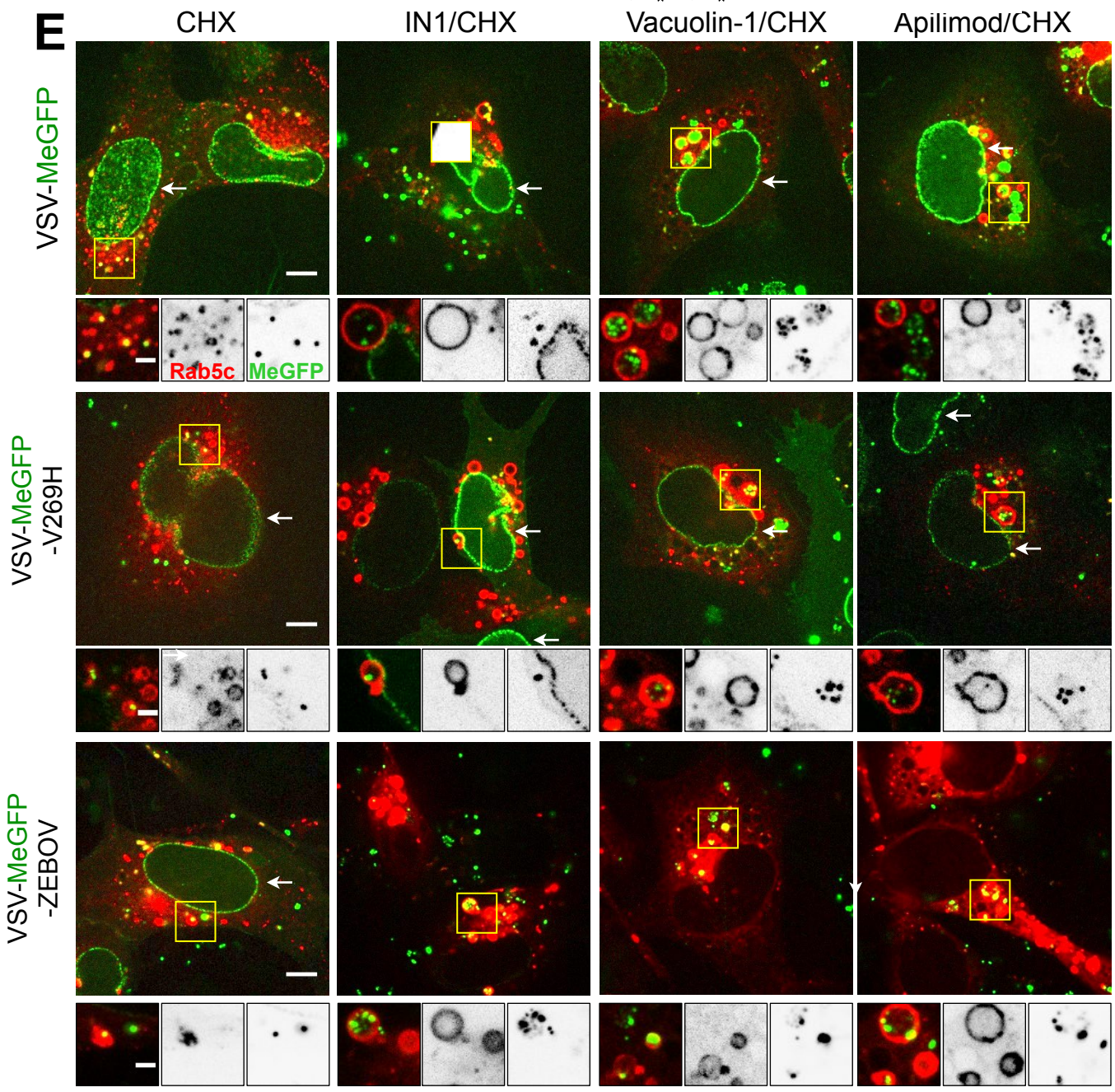
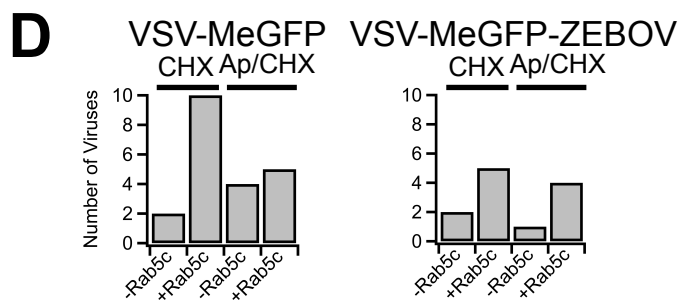
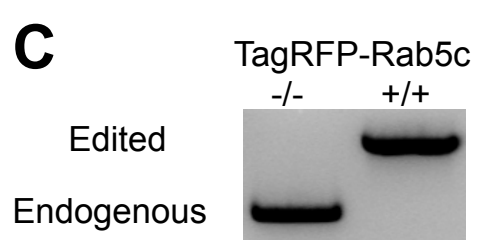
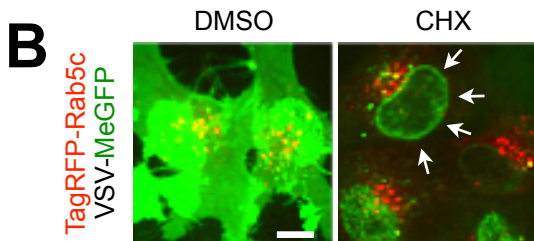
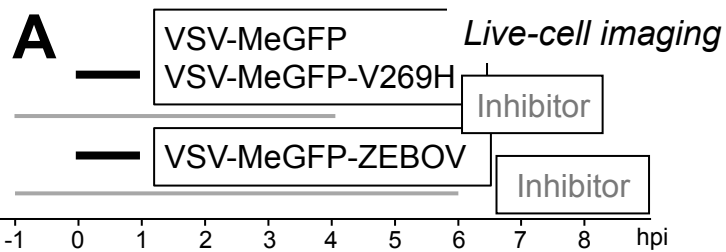


Figure 2



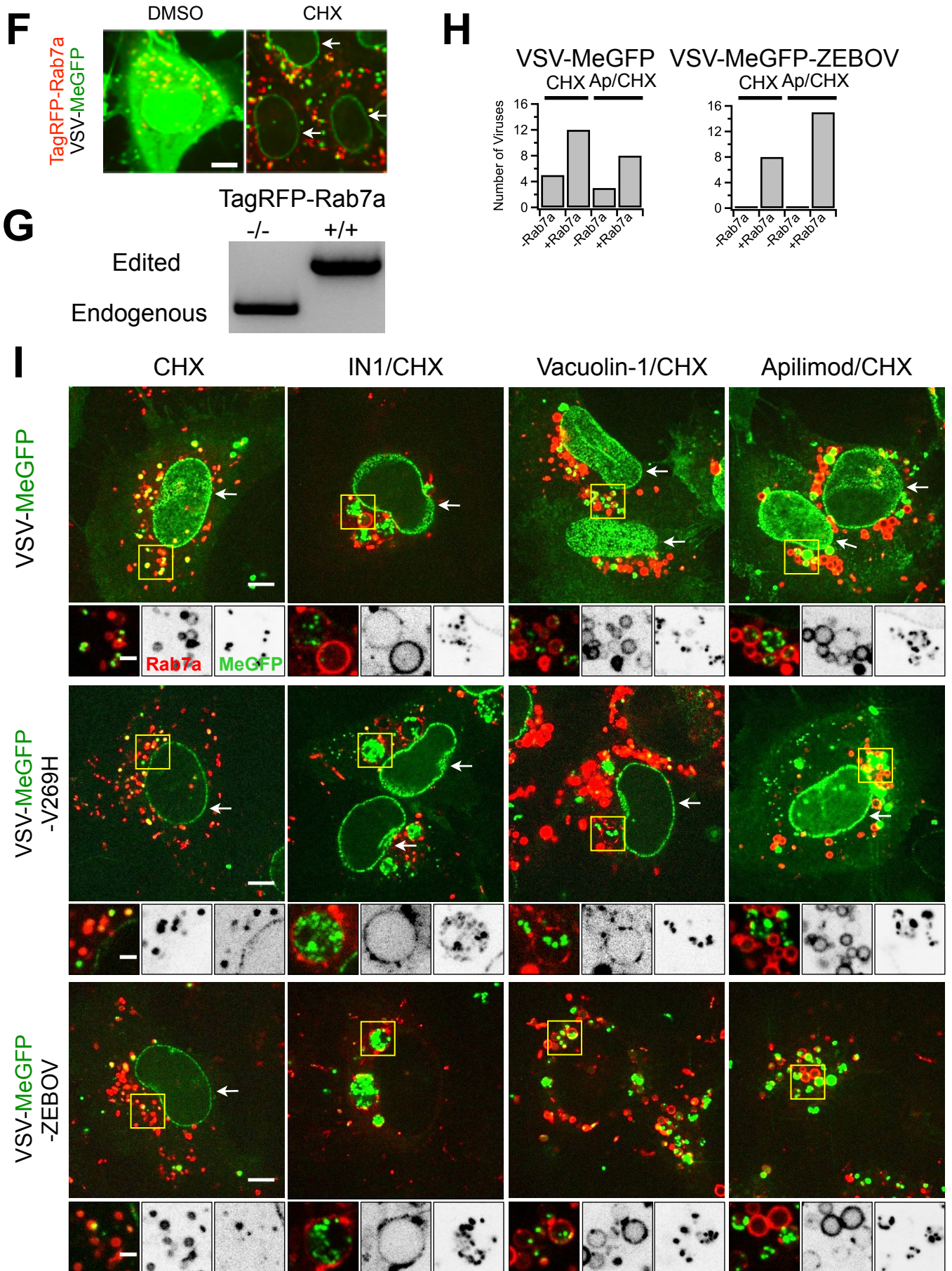


Figure 3

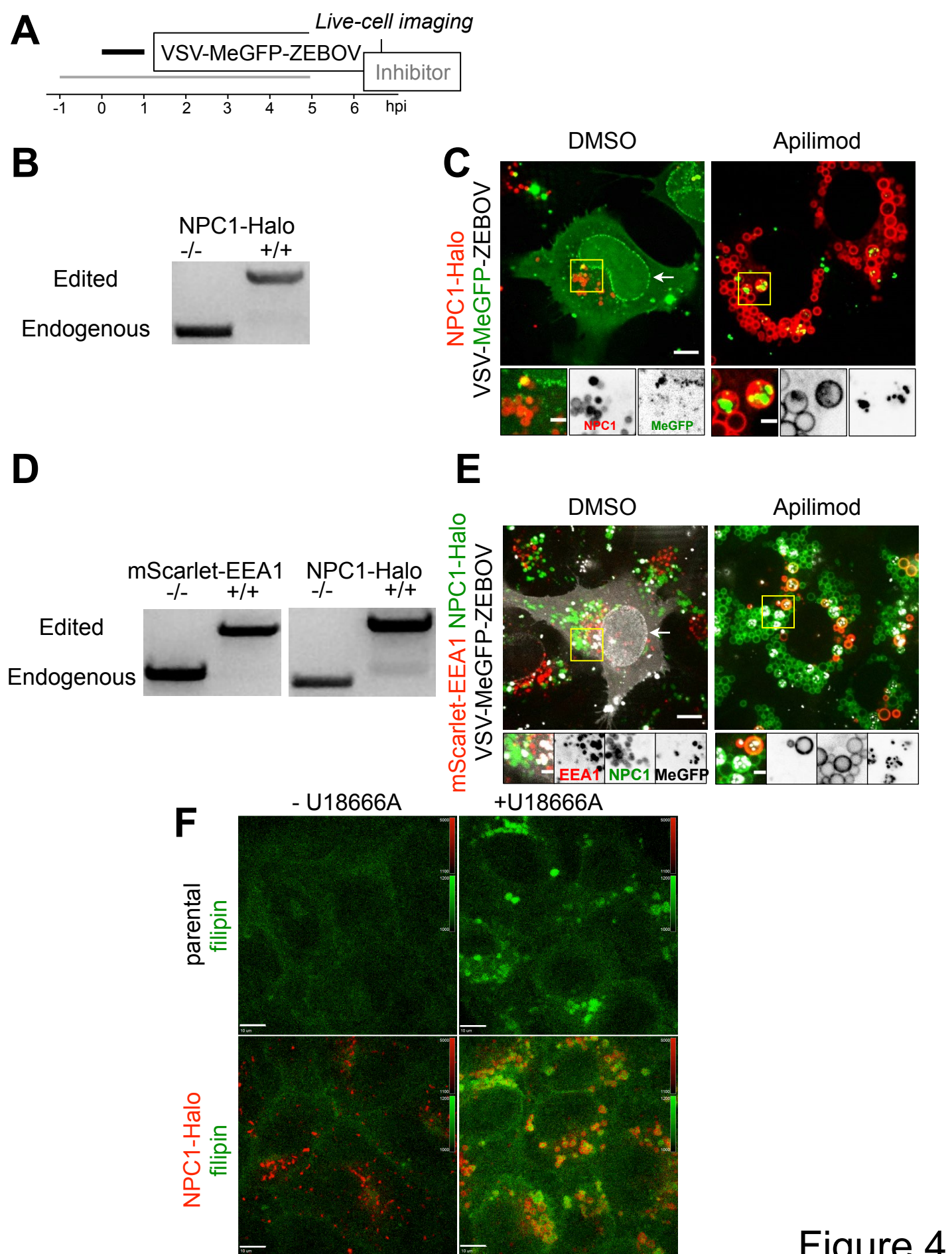
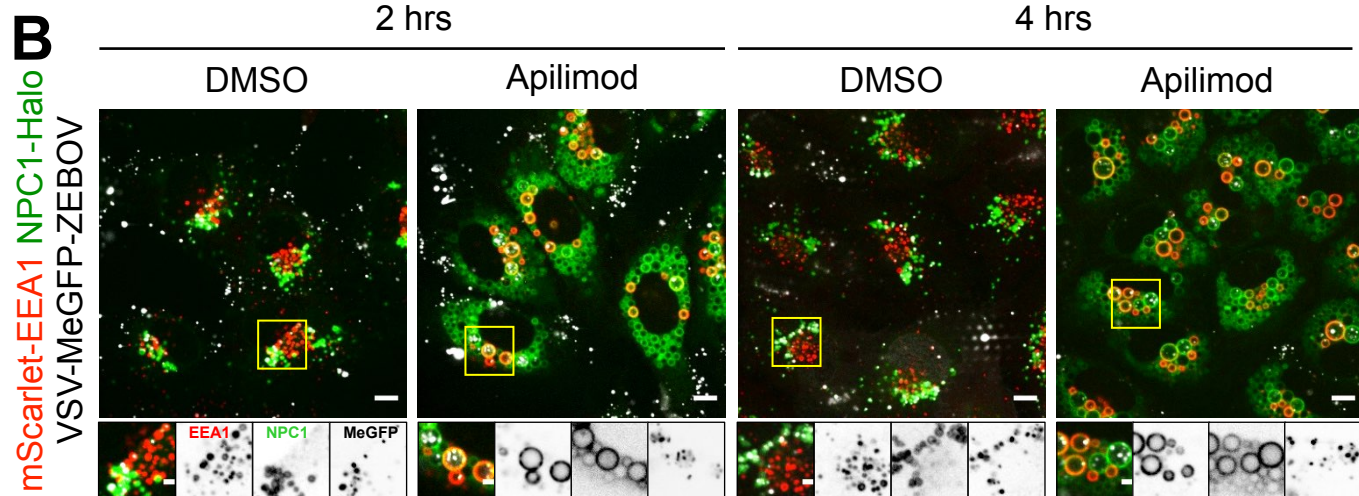
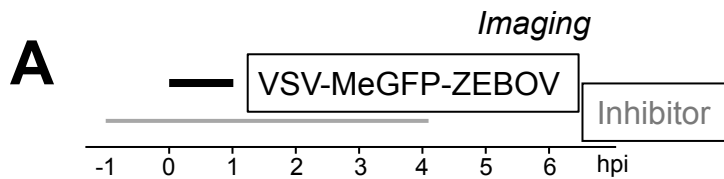


Figure 4



C # of endosomes containing VSV-MeGFP-ZEBOV

	DMSO		Apilimod	
EEA1	9	11	0	0
EEA1/NPC1	2	3	19	16
NPC1	22	25	23	52
# cells	7	6	4	9

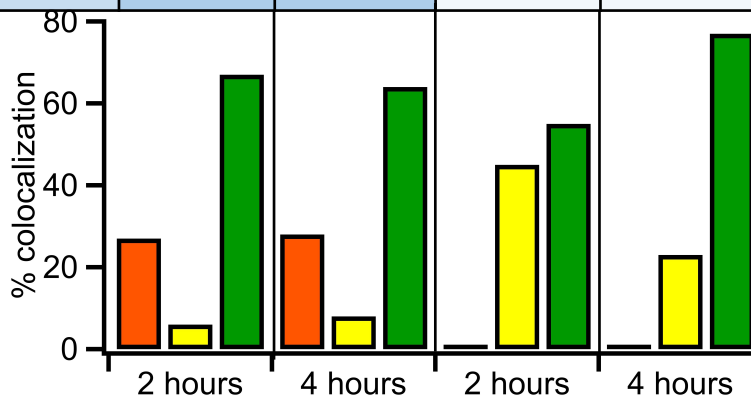


Figure 5

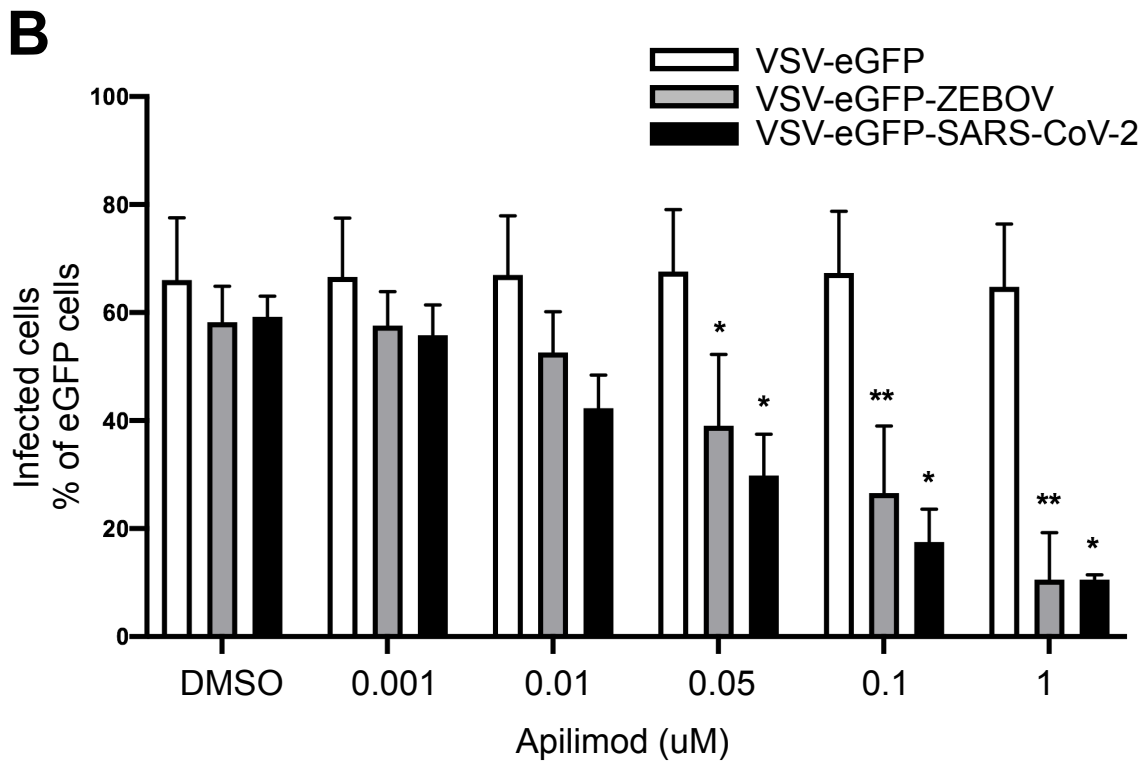
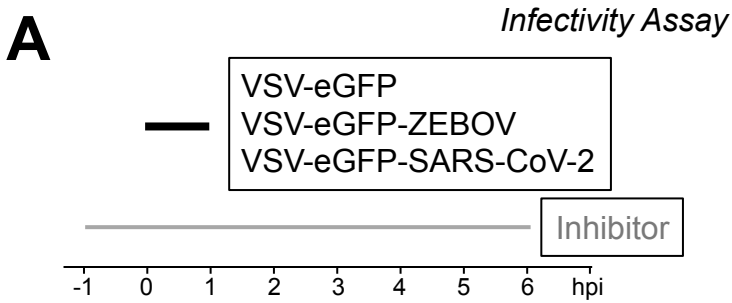


Figure 6

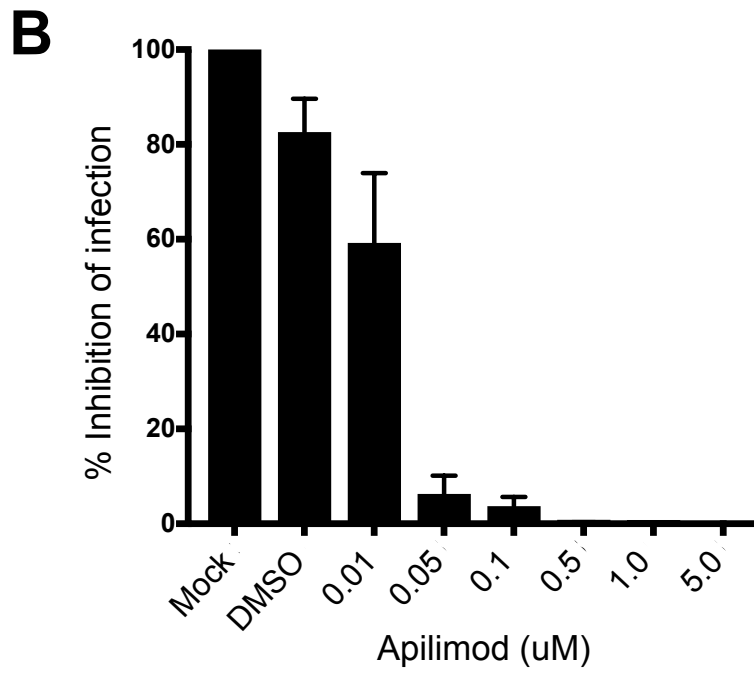
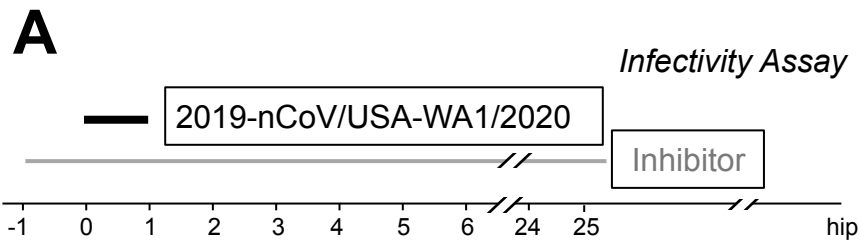


Figure 7

Table I

Primer Description		Sequence
U6 promoter	forward primer	5' GCCGGTACCTGAGGGCCTATTTCCC 3'
	reverse primer	5'ACCTCTAGAAAAAAGCACCGACTCGGTGCCACTTTTTCAAGTTGATAACGGACTAGCCTTATTTAACTTGCTATTTCTAGCTCTAAAAACN NNNNNNNNNNNNNNNNNNNNCGGTGTTTCGTCCTTCCACAAG 3
target sequence for reverse primer	Rab5c	GACCCGCCATTGCCCGTCCA
	Rab7a	TCAAATAAAGGGGAAAAG
	NPC1	TAAATTTCTAGCCCTCTCGC
	EEA1	GGTGGTGGTTAAACCATG
Rab5c	F1	gaattcagctcgggtaccGAGAGAAGTACCTAGGGAAGAAGGATCAG
	R1	TGCCCGTCCAGCTGTAGTG
	F2	CCACTACAGCTGGACGGGCAatggtgtctaaggcgcaagagc
	R2	GGAACCACCAGAACCACCAGAA
	F3	GGTTCGGTGGTTCGGTGGTTCCTGGCGGTCGGGGAGGCGCA
	R3	gtcactctagaggatccccCTCCTACCAAGAGAGTAGAGAAAAG
Rab7a	F1	gaattcagctcgggtaccACTGCTGTGAGCCTTGCCCTTCA
	R1	CCTTCAAATAAAGGGGAAAAGG
	F2	CCTTTTCCCCTTTAGTTTGAAGGatggtgtctaaggcgcaag
	R2	GGAACCACCAGAACCACCAGAA
	F3	TTCTGGTGGTTCGGTGGTTCACCTCTAGGAAGAAAGTGTGCTG
	R3	gtcactctagaggatccccCTCACCAACCTACCACAGAAAT
NPC1	F1	gaattcagctcgggtaccCCTGAGATGAAGGAGTCCAT
	R1	GAAATTTAGAAGCCGTTTCGCGC
	F2	CGCGAACGGCTTCTAAATTTcggaggttctggttctggtgttccGCAGAAATCGGTACTGGCTTTCCA
	R2	GCCGGAAATCTCGAGCGTCGACAG
	R3	CTGTCGACGCTCGAGATTTCCGGCtagccctctcgcaggcatcc gtcactctagaggatccccGCTGTCTAATGAACTTCTAGGTC
EEA1	F1	gaattcagctcgggtaccCTTTGGCTGAAATTAGAAGCAGG
	R1	CATGGTTTAAACCACCACCGGCGC
	F2	CGCCGGGTGGTGGTTAAACCATGgtgagcaagggcgaggcagtgat
	R2	ctgtacagctcgtccatgccgc
	R3	GCGGCATGGACGAGCTGTACAAGggaggttctggtgttctggtgttccTTAAGGAGGATTTTACAGAGGGTAAGAG gtcactctagaggatccccGCTCTAATCTTCTATCCTCAAGGTTTTTC

Table II

Primer Description		Sequence
Rab5c	typing forward	GAGCCTGAAGTTGGGAGACC
	typing reverse	CATGCCCACTCACCTCCAAT
Rab7a	typing forward	GCGGTCACTTCTTTGAGAAAGT
	typing reverse	AAGTGGCAGCACGGACAGTGT
NPC1	typing forward	TCTCCAAAAGAGAGGGGAGAGAGAT
	typing reverse	AAGTTTAGTGTCCCTGTGGTTGCCT
EEA1	typing forward	CATCTGTCAGTTACGGGGGCTG
	typing reverse	CGGCACCACACCCTCCAGCTC